Nonionizing Millimeter-Wave Therapy: Effects on Lung Cancer Spheroids

Helena Tuchinsky , Boris Litvak , Vladimir Freydin , Firas Simaan , Rawad Said , Dhaval Patel , Yosef Pinhasi , Asher Yahalom , Stella Liberman-Aronov *

Posted Date: 25 March 2026

doi: 10.20944/preprints202603.1938.v1

Keywords: millimeter waves; non-ionizing radiation; 3D spheroid; lung cancer; apoptosis; clonogenic assay; W-band

 doi:10.20944/preprints202603.1938.v1

Article

Nonionizing Millimeter-Wave Therapy: Effects on Lung Cancer Spheroids

Helena Tuchinsky [1], Boris Litvak [2], Vladimir Freydin [2], Firas Simaan [2], Rawad Said [2], Dhaval Patel [1], Yosef Pinhasi [2], Asher Yahalom [2,3,4] and Stella Liberman- Aronov [1,*]

[1] Institute of Personal Medicine, Ariel University, Ariel, Israel
[2] Department of Electrical & Electronic Engineering, Ariel University, Ariel, Israel
[3] Center for Astrophysics, Geophysics, and Space Sciences (AGASS), Ariel University, Ariel 40700, Israel
[4] FEL User Center, Ariel 40700, Ariel University, Israel
* Correspondence: stellar@ariel.ac.il; Tel.: (972) 3-937-1431

Featured Application

Millimeter-wave irradiation therapy for noninvasive treatment of human non-small cell lung cancer (NSLC) and breast cancer types.

Abstract

Non-thermal millimeter-wave (MMW) irradiation (75–110 GHz) represents a promising non-invasive strategy for cancer therapy. Lung cancer remains the leading cause of cancer-related mortality worldwide, highlighting the need for alternative therapeutic modalities that can overcome resistance and minimize toxicity. Yet the effects of MMW exposure in physiologically relevant 3D systems remain insufficiently characterized. Here, we evaluated the anti-cancer efficacy of MMW exposure in 3D lung cancer spheroids (NCI-H1299, A549) alongside noncancerous WI-38 fibroblasts. Cells were irradiated using two antenna types—a waveguide (WG; localized, high-power density) and a pyramidal horn (PH; broader coverage, lower power density)—with or without a frequency multiplier to modulate local energy delivery. Acute responses were assessed by XTT viability assays (day 2) and apoptosis (flow cytometry), while chronic effects were evaluated using clonogenic survival (day 10) and senescence markers. MMW exposure reduced cancer cell survival in a time- and power-dependent manner and induced sustained growth inhibition. Apoptosis was markedly higher in cancer cells than in non-cancerous WI-38 cells and was further amplified under power-enhanced conditions. WG irradiation produced strong localized antiproliferative effects, whereas the PH antenna enabled broader coverage while maintaining selective cytotoxicity toward NCI-H1299 cells. Notably, p53-deficient NCI-H1299 cells exhibited up to ~64% apoptosis after 60 min of exposure, whereas WI-38 fibroblasts remained below ~20%, demonstrating robust cancer selectivity. These findings highlight the selective, non-thermal anticancer potential of MMW irradiation in 3D tumor models and provide a mechanistic and experimental foundation for further preclinical optimization of MMW-based therapeutic strategies.

Keywords: millimeter waves; non-ionizing radiation; 3D spheroid; lung cancer; apoptosis; clonogenic assay; W-band

1. Introduction

Despite major advances in cancer research and clinical management, lung cancer continues to pose a profound therapeutic challenge due to its aggressive biology, late-stage diagnosis, and high mortality rates. It remains the most lethal malignancy worldwide, responsible for approximately 1.8–1.9 million deaths annually and representing a substantial proportion of global cancer mortality [1–3]. Lung cancer is also among the most frequently diagnosed cancers, with over two million new

 doi:10.20944/preprints202603.1938.v1

cases reported each year, and is characterized by poor overall survival, particularly in advanced stages [1,2]. Non-small cell lung cancer (NSCLC), the predominant histological subtype, encompasses genetically and phenotypically distinct variants, including p53-deficient, KRAS-mutant, and EGFR-mutant tumors, which exhibit variable proliferation rates, apoptotic responses, and metabolic profiles. The five-year survival rate for NSCLC remains below 25% across all stages, reflecting persistent limitations of current treatment strategies [4]. Although targeted therapies and immunotherapy have improved outcomes for selected patient populations, treatment resistance and systemic toxicity remain significant clinical obstacles [5].

Despite innovations in therapeutic approaches—including biologic agents, chemotherapeutic agents, and radiation therapy—existing treatments often demonstrate toxicity while lacking selectivity for both healthy and cancerous tissues [6]. Additionally, the unavailability of precise models that faithfully simulate the human tumor microenvironment has limited the development of effective therapies. Traditional two-dimensional (2D) cell cultures provide insights into tumor cell growth but fail to capture tumor-stroma interactions and cell–cell interactions. *In vivo* animal models are more relevant, but they often fail to adequately predict clinical outcomes, are time-consuming, and may involve ethical constraints. Therefore, three-dimensional (3D) *in vitro* models, such as tumor spheroids, have gained increasing interest to bridge the gap between 2D cell culture and animal models. Tumor spheroids replicate the architecture of the tumor microenvironment and allow better modelling of cell interactions and response to therapies [7,8].

2D Millimeter-Wave Studies and Anticancer Effects

Previous studies have extensively explored the effects of millimeter-wave (MMW) irradiation on cancer cells using 2D models. As early as 2004, Radzievsky et al. [9] demonstrated that MMW therapy (MMWT) could inhibit melanoma growth, and 'naloxone' pretreatment—a competitive opioid receptor antagonist—completely abolished this effect, indicating that endogenous opioids contribute to MMW-mediated cellular responses. Broadband MMW spanning 53.57–78.33 GHz inhibited the proliferation of human melanoma cells, whereas single-frequency exposures at 51.05 GHz or 65.00 GHz did not significantly alter growth [10]. Low-power MMW irradiation at the frequencies 42.2 GHz and 53.57 GHz did not alter the doubling time or cell cycle of RPMI 7932 melanoma cells [6,11,12]. Broadband MMW exposure induced morphological changes associated with osmotic transmembrane balance and cellular water content. More recent studies demonstrated that MMW reduces A375 melanoma cell viability by activating caspase-3 and caspase-8, promoting apoptosis [12]. Frequency- and irradiation time–dependent antiproliferative effects were confirmed in RPMI 7932 cells [14,15]. Collectively, these studies provide mechanistic evidence for the anticancer potential of MMW irradiation in 2D models, supporting its translation to more complex 3D systems.

Building on these 2D findings, recent studies [16–20]—have demonstrated that lung cancer cells exhibit genotype-dependent sensitivity to MMW irradiation, underscoring the need to investigate selective anticancer effects in physiologically relevant 3D tumor models. Compared with conventional 2D cultures, 3D spheroids more faithfully replicate tumor architecture, including cell–cell and cell–matrix interactions, nutrient and oxygen gradients, and differential energy penetration, providing a more accurate platform for evaluating therapeutic strategies such as MMW irradiation [7,8,19].

In this study, we irradiated lung cancer cells (NCI-H1299 and A549) in a 3D hemispherical droplet model over acute (day 2) and chronic (day 10) exposure periods, alongside noncancerous lung fibroblasts (WI-38) as controls. The MMW radiation, in the W-band (75–110 GHz) regime, was transmitted using two types of antennas: a waveguide (WG) antenna that produced a highly focused beam (0.0437 cm^2; ~0.6 mW/cm. The MMW radiation, in the W-band (75–110 GHz), was delivered using two types of antennas: a waveguide (WG) antenna, producing a highly focused beam (0.0437 cm^2; ~0.6 mW/cm^2), and a pyramidal horn (PH) antenna, providing a broader irradiation area (0.33 cm^2) but with approximately tenfold lower power density (~0.08 mW/cm^2). To increase the PH antenna's power density, a frequency multiplier was incorporated, and the operational frequency

 doi:10.20944/preprints202603.1938.v1

range was narrowed to 90–96 GHz. Using this configuration without attenuation, the power density remained ~0.08 mW/cm², whereas with the multiplier and optimized setup, the power density reached ~4.9 mW/cm². Due to the pyramidal geometry of the horn, the power distribution was non-uniform, with the highest intensity at the center and gradually decreasing toward the edges. This configuration allowed systematic evaluation of both localized (WG) and wide-area (PH) exposure setups.

The study aimed to assess the selectivity and specificity of MMW irradiation across lung cancer subtypes, identify optimal irradiation conditions, and explore underlying cellular mechanisms in a physiologically relevant 3D context. Given the distinct tissue origins and genetic mutation profiles of lung cancer cells, we hypothesized that each type and subtype may require tailored irradiation parameters to achieve optimal therapeutic efficacy.

2. Results

2.1. 3D Cell Model of The Study and Irradiation Geometry

In previous studies, we demonstrated a significant anti-cancer effect of MMW irradiation at a PD of 0.2 mW/cm² in 2D human (lung) cancer and budding yeast models (*Saccharomyces cerevisiae*) [13,15]. Importantly, MMW-induced effects were significantly stronger in cancer cells than in normal cells of the same tissue origin. In the present study, we extended these findings to a physiologically relevant 3D tumor-like model. We systematically evaluated the efficacy of irradiation and optimal irradiation conditions of MMW exposure over a wide PD range (~ 0.6–5 mW/cm²) on spheroid sizes. Lung cancer (NCI-H1299 and A549) cell lines were examined alongside non-cancerous (lung cell)controls (WI-38) to assess specificity. 3D multicellular models are recognized as providing a more physiologically relevant system for studying tumor biology. To better understand the geometry of the system, we performed a Computational Spheroid Modelling Analysis. Figure 1 shows the MMW irradiation setup, the structure model of a 3D spheroid, and its properties. In Panel A, a WG antenna delivers a focused MMW beam to a hemispherical 3D tumor spheroid (maintained at approximately 15 °C). The cells with densities from 5000 cells/μL to 250,000 cells/μL in growth medium were loaded in the middle of 35 mm cell culture plates, forming a dome-shaped hemispherical structure. The spheroids were maintained at approximately 15 °C by placement on a metal table positioned on ice, ensuring that all observed effects were non-thermal and protecting cells from thermal stress during irradiation. MMW irradiation was applied from above using a WG antenna (75-110 GHz range, PD-0.575 mW/cm²), enabling localized, near-field exposure of the hemispherical droplet.

Due to the physical properties of MMW, energy absorption decreases exponentially with depth according to the formula: $I=I_0e^{-z/l}$, where l represents the penetration depth (~1 mm). Consequently, superficial cell layers receive the highest energy dose, while deeper layers experience progressively attenuated exposure. Panel B presents a computational diagram that illustrates a physical model of a 3D tumor spheroid, assuming the spheroid adopts the shape of a perfect hemisphere with an average cell area of ~1500 μm². The calculated radius is approximately 1.68 mm and 2.08 mm for the two drop volumes used.

 doi:10.20944/preprints202603.1938.v1

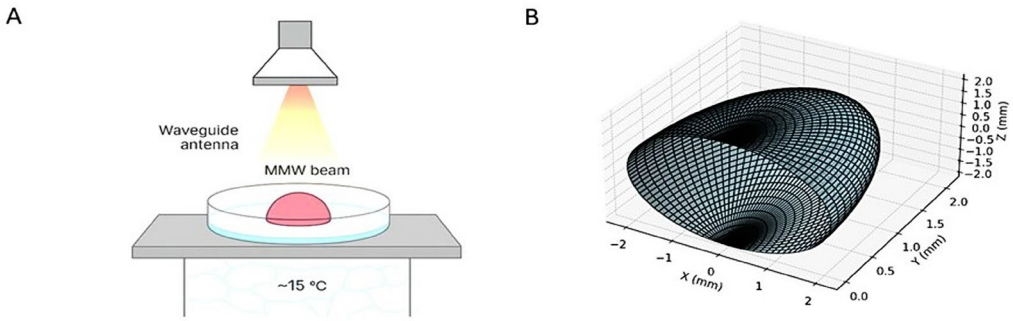

C

Parameters of the 3D model	Value	
Total volume	10 µL = 10 mm³	20 µL = 20 mm³
Hemisphere radius	~1.68 mm	~2.08 mm
Number of cells	5,000	250,000
Average cell area	1500 µm²	1500 µm²
Estimated cell height	~38.7 µm	~38.7 µm
Estimated single cell volume	~58,050 µm³	~58,050 µm³
Total volume of cells	~0.3 mm³	~14.5 mm³
Volume occupied by cells	~2.9% of total	~72.5% of total

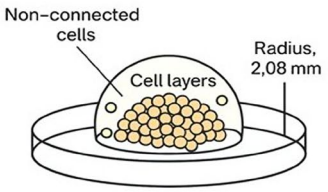

Figure 1. MMW irradiation setup, modelled energy distribution, and structural organization of a hemispherical tumor spheroid. (**A**) Schematic of the MMW irradiation setup. A WG antenna delivers a focused MMW beam onto a hemispherical tumor spheroid maintained at ~15 °C. (**B**) Computational 3D model showing a perfect hemisphere formed by 250,000 cells in 20 µL of medium based on geometry and total mass distribution (**C**). Summary of the parameters for physical models. (**D**). Structural representation of the hemispherical spheroid (radius 2.08 mm) composed of compact cell layers and peripheral non-connected cells.

Panel C provides the geometrical parameters of the model (e.g., volume, radius, cell density, surface curvature). Panel D depicted the structural model, which assumes a compact and uniform cell distribution, consistent with gravity-assisted self-assembly typically observed in hanging-drop or low-adhesion culture systems. The spheroid (radius: 2.08 mm) contains multiple compact tumor cell layers forming the dome, while loosely attached, non-connected cells occupy the outer surface. These values align with the empirical 3 × 4 mm hanging-drop footprint shown in Table 1. This architecture closely mimics *in vivo* micro-tumor geometry and provides a controlled system for evaluating how MMW energy gradients influence apoptosis, metabolic stress, and viability across different cellular layers.

Table 1. Estimated energy deposition and depth-dependent distribution in semispherical spheroids under MMW Irradiation using a WG antenna (α = 0.5).

Spheroid radius	Duration	Total energy deposited (mJ)	Equivalent power (mW)	Estimated energy range (surface → base, mJ)
1.68 mm	15 min	942 – 1,566	1.05 – 1.74	942 – 471 → 1,566 – 783
	30 min	1,884 – 3,132		1,884 – 942 → 3,132 – 1,566
	60 min	3,768 – 6,264		3,768 – 1,884 → 6,264 – 3,132

 doi:10.20944/preprints202603.1938.v1

2.08 mm	15 min	1,494 – 4,158	1.66 – 2.77	1,494 – 747 → 4,158 – 2,079
	30 min	2,988 – 8,316		2,988 – 1,494 → 8,316 – 4,158
	60 min	5,976 – 16,632		5,976 – 2,988 → 16,632 – 8,316

2.2. Depth-Dependent Energy Deposition

Geometric parameters required for understanding cell-packing estimates for hemispherical tumor spheroids. Since the drop containing cells spreads in an elliptical shape rather than circular, the footprint imposes a fixed geometric constraint, which limits it to approximately R_{dome}≈1.6–2.1 mm. Under this constraint, the spheroid cannot expand laterally beyond the footprint, and additional cells must therefore accumulate vertically, forming a multilayered 3D structure. Using this geometry, the surface capacity parameter can be estimated. The curved surface area of a hemisphere with radius R_{eq} is:

$$R_{eq} = \sqrt{ab}$$

Where, a=2.0 mm and b=1.5 mm — the semi-axes of the ellipse.

$$R_{eq} = \sqrt{2.0 \times 1.5} \approx 1.73\ mm$$

This equivalent radius defines the maximum lateral extent of the spheroid, which is similar to our previous calculation (1.68-1.8mm).

Assuming a hemispherical geometry, the available curved surface area A_{hemi} is:

$$A_{hemi} = 2\pi R_{eq}^2$$

$$A_{hemi} = 2(1.73\ mm)^2 \approx 18.8\ mm^2 = 1.88 \times 10^7\ \mu m^2$$

The maximum number of cells that can occupy the hemispherical surface is given by:

$$N_{surface} = \frac{A_{hemi}}{A_{cell}}$$

Assuming an average projected cell area of ~1500 μm²: Thus, approximately 12,500 cells can be accommodated on the spheroid surface as a single layer.

$$N_{surface} = \frac{1.88 \times 10^4}{1500} \approx 1.25 \times 10^4\ cells$$

This is the maximum number of cells that can form a single packed monolayer on the drop surface. Accordingly, a drop containing ~ 5,000 cells per 10 μL forms a surface-packed monolayer-like spheroid, whereas a 250,000-cell spheroid in a 20 μL drop with the same 3 × 4 mm footprint corresponds to ~20 cell layers on average—a highly compact, strongly 3D multilayered dome whose lateral radius remains constrained (~1.6–1.8 mm) and whose growth is expressed primarily as increased height.

Schematically, this data is shown in Figure 2A, with very high cell numbers. The droplet footprint may deviate slightly from the idealized fixed geometry, allowing limited lateral expansion and reducing the effective number of vertical layers relative to the purely geometric estimate. However, because droplets were deposited on plastic Petri dishes cooled (from below 4 °C, metal support), the contact area was largely constrained by wetting and temperature, such that increasing cell number predominantly resulted in vertical thickening rather than lateral spreading.

 doi:10.20944/preprints202603.1938.v1

A

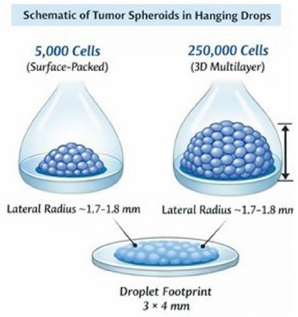

B

Relationship between total cell number and spheroid geometry

Total cells	Packing regime	Effective lateral radius
5,000	Surface-dominated (quasi-2D)	~1.6–1.8 mm
250,000	Volume-dominated (3D multilayer)	~1.7–2.1 mm

C

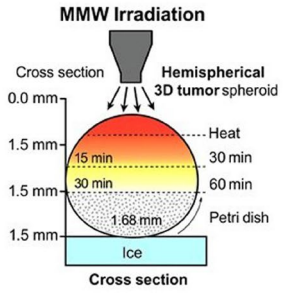

D

Depth (mm)	Absorbed Intensity (% of surface)	Accumulated Effect		
		at 15 min	30 min	60 min
0.1	~95%	High	Higher	Maximal
0.5	~60%	Moderate	High	Very High
1.0	~25%	Low	Moderate	High
1.5	~5–10%	Minimal	Low	Moderate
1.68 (center)	~3%	Negligible	Low	Moderate (via heat diffusion)

Figure 2. (A) Cell-Number–Dependent Spheroid Architecture. Schematic representation of tumor spheroids formed in hanging droplets. A small, surface-dominated spheroid composed of ~5,000 cells (10 μL droplet) and a larger, multilayered spheroid composed of ~250,000 cells (20 μL droplet) are shown. In both cases, lateral dimensions are constrained by the experimentally observed droplet footprint (~3 × 4 mm), resulting in a lateral radius of approximately 1.7–1.8 mm, while vertical growth is determined by total cell number and uniform packing. Surface-packed cells (5,000 cells) vs. multilayered spheroid (250,000 cells). Vertical growth is indicated by height arrows**. (B)** Relationship between total cell number and spheroid geometry. **(C-D)** Distribution and attenuation of MMW irradiation in the range 75-110 GHz in a 3D tumor spheroid. **(C)** Schematic of the experimental setup showing MMW irradiation applied to a hemispherical 3D tumor spheroid (diameter: 1.68 mm) placed in a petri dish with ice underneath to maintain a cold base. Heating durations vary by depth: 15 minutes at the top, 30 minutes in the middle, and 60 minutes at the bottom. (**D)** The table illustrates a time-dependent but depth-attenuated distribution of absorbed MMW energy within a 1.68-mm spheroid, with maximal deposition at the surface and progressively reduced exposure toward deeper layers, consistent with exponential penetration decay.

Figures 2C,D illustrate the theoretical distribution of absorbed MMW energy within a hemispherical spheroid positioned on a cold base. Figure 2C schematically represents the differential exposure of spheroid layers, with effective irradiation times of 15 min at the surface, 30 min in the middle, and 60 min at the base. Figure 2D summarizes the estimated absorbed energy within a spheroid of 1.68 mm radius as a function of irradiation duration and depth. Calculations assume direct near-field irradiation, constant average PD, and a 50% absorption factor (α = 0.5). Total deposited energy increases linearly with exposure time, whereas energy distribution remains depth-dependent due to exponential attenuation. At shorter irradiation durations (e.g., 15 min), energy deposition is largely confined to superficial layers. Prolonged exposure (30–60 min) allows biologically relevant energy levels to reach deeper spheroid layers despite continued attenuation. This gradient provides a mechanistic explanation for observed layer-specific biological responses, with stronger stress responses expected in superficial cells and delayed or attenuated effects in inner layers.

 doi:10.20944/preprints202603.1938.v1

2.3. Quantitative Energy Estimates

Using a WG antenna (see properties Figure 9 and Table 3), the irradiation range was delivered at power levels of 0.38–0.63 mW, corresponding to an average PD of 0.6 mW/cm², respectively. Assuming the absorption of energy, the estimated deposited energy increased linearly with irradiation time, while equivalent power remained constant. The estimated energy range from the surface to the base of the spheroid is presented in Table 1, providing a rough gradient for each spheroid size and irradiation duration. For spheroids with a radius of 1.68 mm, deposited energy ranged from ~942–1566 mJ after 15 min to ~3,768–6,264 mJ after 60 min. For larger spheroids (2.08 mm radius), energy deposition ranged from ~1,494–4,158 mJ after 15 min to ~5,976–16,632 mJ after 60 min. Importantly, the energy deposition was non-uniform. Surface-facing cells received the highest exposure, while deeper layers experienced attenuated yet biologically effective doses. This gradient is critical for interpreting differential cellular responses within the 3D structure.

2.4. Effect of Cell Density on Cell Viability after MMW Irradiation

To optimize the cell density required for effective MMW irradiation of the cancer cells, the NCl-H1299 (lung cancer) cells at three different cell densities (i.e., 5.0 × 10^3 cells/10 µL, 1.0 × 10^4 cells/10 µL, and 2.0 × 10^4 cells/10 µL) were exposed to MMW using a WG antenna. The WG antenna provided highly localized irradiation (with aperture = 0.44 cm²) over a broad frequency range (75–110 GHz) with an average PD of ~0.6 mW/cm. Following the irradiation, the biological effects were assessed using XTT and colony formation assays at Day 2 (acute effects) and Day 10 (chronic effects), enabling evaluation of both immediate and long-term impacts on cell proliferation and survival. Positive (doxorubicin-treated) and negative (untreated/sham-irradiated) controls were included in all experiments.

The biological effect of non-thermal MMW irradiation on the tested cancer cells are depicted in Figure 3. Figure 3 shows that the highest % cell survival (65%) occurred at a cell density of 1.0 × 10^4 cells, when irradiated for 15 minutes. This was followed by a % cell survival observed at a density of 2.0 × 10^4 cells, with irradiation durations of both 15 minutes and 30 minutes on day 2. The lowest %cell survival (i.e., 26.2 %) was when 5 × 10^3 cells were exposed to irradiation for 30 min. On the other hand, on day 10, the highest %cell survival (42%) was observed for 2 × 10^4 cells/10 µL cell density exposed to 15 min, and the lowest %cell survival (6.2%) was observed in 5 × 10^3 cells/10 µL cell density exposed for 60 min.

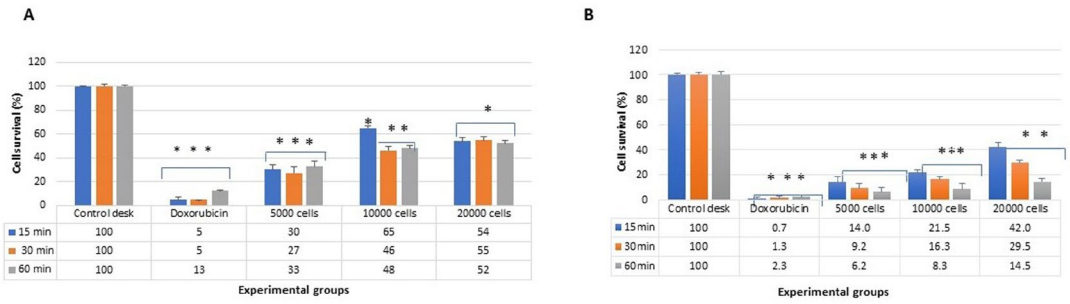

Figure 3. (A) Acute effects of MMW irradiation on NCl-H1299 cells measured on Day 2 using the XXT assay. **(B)** Chronic effects were measured on Day 10 using the colony formation assay (CFA). Error bars represent the standard deviation from four biologically independent experiments. Statistical analysis was performed using one-way ANOVA. Significance is indicated as follows: $p < 0.05$ (*), $p < 0.01$ **(**)**, and $p < 0.001$ (**), comparing irradiated groups to control/sham groups.

The findings suggested that the cell density in 3D droplets plays a crucial role in modulating the cell viability response of NCl-H1299 cells to MMW irradiation. Optimal survival was achieved at a density of 1.0 × 10^4 cells/10 µL following short-term exposure (15 min), suggesting that intermediate

 doi:10.20944/preprints202603.1938.v1

cell concentrations may enhance resistance to MMW-induced stress. In contrast, lower cell densities (5.0×10^3 cells/10 µL) were more susceptible to irradiation, particularly under prolonged exposure, as observed by the significant reduction in survival on both Day 2 and Day 10.

2.5. Comparison of Antenna Systems and Power Densities on Cell Viability

Four antenna-amplifier configurations were evaluated on a 3D tumor-like model, with NCl-H1299 cells (see Methods, Table 3 and Figure 4). Exposure using the PH antenna equipped with a frequency multiplier without attenuation generated an average PD approximately 10-fold higher than that produced by the WG antenna, although within a narrower frequency sweep (90–96 GHz) . Under these conditions, a pronounced cytotoxic response was observed in NCI-H1299 cells (Figure 4). Acute effects measured (day 2) post-irradiation revealed 50–70% reductions in %cell survival for both the WG antenna and the PH antenna (7 × 4.7 mm) with a multiplier without attenuation. The strongest cytotoxic effect was observed in cultures seeded at 5000 cells/10 µL. In contrast, irradiation using the PH antenna with a multiplier and attenuation did not significantly affect %cell survival at the tested densities (data not shown). This lack of effect may be attributed to the larger irradiation area combined with substantially lower PD compared with the WG antenna configuration.

Long-term survival assessed using the colony formation assay (CFA) demonstrated a marked reduction in clonogenic potential at a cell density of 5000 cells/10 µL, with only 10 ± 0.61%, 17 ± 1.5%, and 33 ± 2.1% of cells forming colonies after 10 days of irradiation ($p < 0.05$). This result indicates that MMW-induced cytotoxic effects are prolonged and largely irreversible under the tested experimental conditions.

Overall, these results demonstrate that antenna configuration, frequency range, and attenuation significantly influence the cytotoxic response of NCI-H1299 cells, particularly at higher initial cell densities. Figure 4 illustrates how variations in frequency range, power density, and attenuation (mentioned in Table 3) affect cellular responses across different cell densities and experimental conditions.

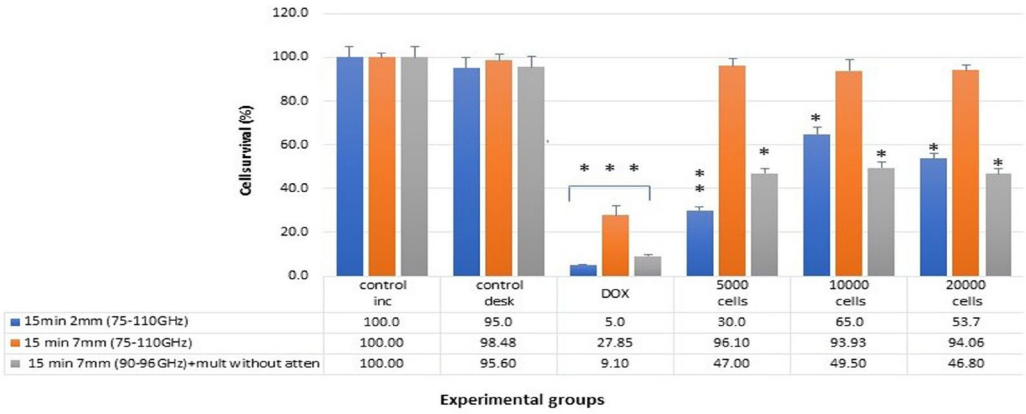

Figure 4. Quantification of the measured cellular response across six experimental groups. Control incubator: cells maintained in the incubator throughout the experiment (negative control). Control table: cells transported and kept outside the incubator during the irradiation period (sham control). Doxorubicin-treated cells: positive control. Cells were irradiated for 15 min under three exposure conditions: WG probe (2.5 × 1.75 mm; aperture 4.37 mm²) at 75–110 GHz (0.975 mW; blue bars); PH antenna (7 × 4.7 mm; aperture 32.9 mm²) at 75–110 GHz with attenuation (0.38–0.08 mW; orange bars); and PH antenna at 90–96 GHz without attenuation (4.8 mW; grey bars). Data are presented as percentages relative to control groups. Statistical analysis was performed using one-way ANOVA, with significance defined as $p < 0.05$, $p < 0.01$, and $p < 0.001$.

 doi:10.20944/preprints202603.1938.v1

2.6. Effect Of MMW Irradiation by a Pyramidal Antenna on Viability and Apoptosis of the Lung Cancer Cells with Distinct Genotypes and Phenotypes

The PH antenna with multiplier, operated without attenuation, was used to expose a high-density 3D tumour-like model containing 250,000 cells to MMW irradiation. WI38 cells were also subjected to the same treatment and served as the control group for two genetically distinct NCl-H1299 and A549 lung cancer cells (as mentioned in the Materials and Methods section). The exposure durations were 15, 30, and 60 min. The acute effects were assessed on day 2 using the XTT assay, while the chronic effects were evaluated on day 10 using CFA.

The three cell lines represent distinct genetic and phenotypic backgrounds relevant to lung biology. Briefly, the NCL-H1299 cells are p53-null, highly proliferative NSCLC cells with an aggressive phenotype. A549 cells carry wild-type p53 and display a more epithelial, differentiated phenotype with slower growth. WI-38 fibroblasts are non-cancerous, diploid lung cells with intact cell-cycle control and low baseline proliferation, serving as a model of normal lung tissue. Together, these models enable evaluation of cancer-specific *versus* normal-cell responses to MMW irradiation. We examined the effect of a PH antenna equipped with a multiplier (7 × 4.7 mm, PD = 4.9 mW/cm²) using a 3D tumor-like model (25,000 cells/20 µL). NCL-H1299, A549, and WI-38 cells were irradiated for 15, 30, or 60 min. Acute effects were measured after 2 days using XTT, and chronic effects were evaluated after 10 days using CFA. The results are shown in Figure 5.

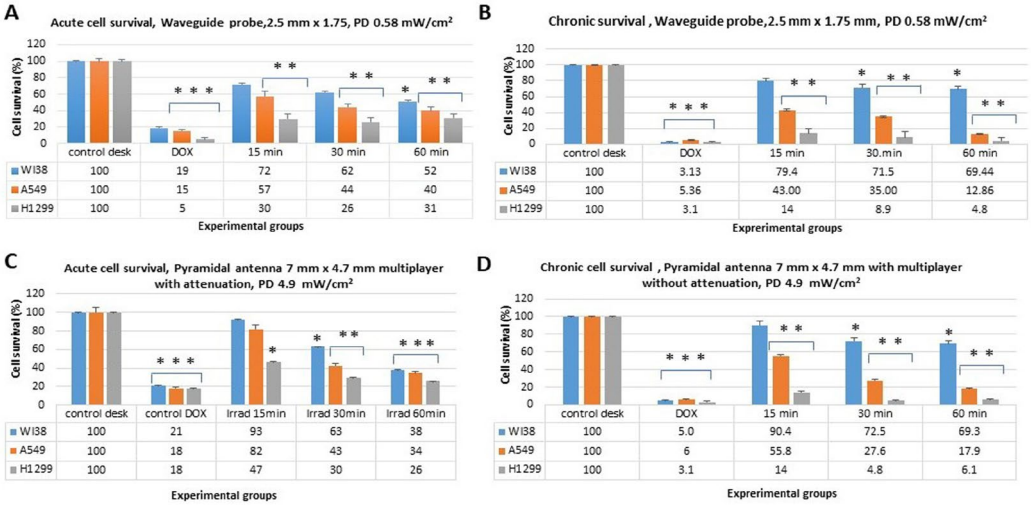

Figure 5. (A) Acute cell survival and **(B)** Chronic cell survival of NCL-H1299, A549, and WI38 cells using a WG antenna 2.5 mm × 1.75 mm with PD 0.58 mW/cm², **(C)** Acute cell survival and **(D)** Chronic cell survival of NCL-H1299, A549, and WI38 cells using a PH antenna 7 mm × 4.7 mm and a multiplier with PD 4.9 mW/cm². Data are presented as mean percentage cell survival of three independent experiments. Error bars represent the standard deviation from four biologically independent experiments. Statistical analysis was performed using single-factor ANOVA. Significance is indicated as: $p < 0.05$ (*), $p < 0.01$ (**), and $p < 0.001$ (***), compared with sham-irradiated controls.

The highest %cell survival of NCL-H1299 was observed after 15 min irradiation, both on day 2 (47%) and day 10 (17%), and the lowest % cell survival after 60 min of irradiation on both day 2 (26%) and day 10 (6.7%). A similar trend was observed in A549 and WI38 (see Figure 5A). On the other hand, the %cell survival of WI38 was higher (day 2 → 93%, and day 10 → 90%) compared to A549 (day 2 → 82%, and day 10 → 55.8%) and NCL-H1299 (day 2 → 47%, and day 10 → 17%) after 15 min of irradiation, indicated that, MMW irradiation was safer for normal cells. The trend remains unchanged after 30 min and 60 min of exposure. Our observations indicate that there was no significant anti-proliferative effect on lung cancer cells following irradiation with a PH antenna measuring 7 × 4.7 mm, utilizing a sweeping frequency range of 75-110 GHz (data not shown).

 doi:10.20944/preprints202603.1938.v1

Notably, the PD generated by this antenna was an order of magnitude lower than that of the WG antenna operating within the same frequency range. Consequently, the delivered power was less concentrated, and the radiation was more diffuse—both due to structural differences and the larger irradiated area produced by the PH antenna (see Table 3). However, we observed a partial anti-proliferative effect with the utilization of the same PH antenna in a narrower frequency range of 90-96 GHz (data not shown), although these irradiation conditions did not achieve statistical significance in their impact on the cells. In accordance with the specified conditions, a significant effect was observed in the %cell survival of lung cancer cells (NCl-H1299 and A549) compared to lung fibroblast cells (WI38) (Figure 5). The %cell survival on day 2 for NCl-H1299 was 30%, 26% and 31% for 15, 30 and 60 min of exposer, while the %cell survival on day 2 for A549 cells was 57%, 44% and 40% for 15-, 30- and 60-min exposer, respectively. On the other hand, for WI38, cell survival was 72%, 62% and 52% for same time duration.

A similar trend was observed on day 10 across all tested cells and exposure times (see Figure 5B and D). It is evident from the above results that exposure to MMW can reduce cell survival rates without affecting normal cells. It is reported that MMW enhances apoptosis through mechanisms involving the downregulation of anti-apoptotic proteins and the generation of reactive oxygen species (ROS) [13]. To investigate this mechanism, apoptosis was evaluated in lung cancer and lung fibroblast cells using flow cytometry (see the Materials and Methods section). The result of apoptosis is depicted in the following table (Table 2).

Table 2. Percentage apoptosis of lung cancer and lung fibroblast cells following MMW irradiation (90-96 GHz) using a 7 mm × 4.7 mm PH antenna for 30 min and 60 min. Cells were immediately stained following irradiation for apoptosis and necrosis using Annexin V and *P*ropidium *I*odide (PI), respectively. Each sample contained 1,000,000 cells, and *the* experiments were performed in triplicate ($n = 3$).

Cell type	%Apoptosis ± SD			
Lung cancer cells	Exposure time with attenuation		Exposure time without attenuation	
	30 min	60 min	30 min	60 min
NCL-H1299 (p53 deficient)	38 ± 0.05	52 ± 0.6	25 ± 0.6	64 ± 0.6
A549 (p53 wild type)	31.4 ± 0.8	28 ± 1.2	41 ± 0.5	38 ± 1.2
WI38 (noncancerous lung fibroblast)	12.8 ± 0.4	14 ± 0.7	16 ± 0.7	19 ± 0.5

It can be seen from the above table (**Table 2**) that the exposure using a PH antenna without a multiplier resulted in 38 ± 0.5% apoptotic NCL-H1299 cells after 30 min and 52 ± 0.6% after 60 min, whereas, WI-38 cells exhibited significantly lower apoptosis (12.8 ± 0.4% and 14 ± 0.7%, respectively). When PH antenna with a multiplier was used, apoptosis in NCl-H1299 cells increased markedly to 64 ± 0.6% after 60 min. A549 cells were more resisted as compared to NCl-H1299 and showed moderate apoptosis, while WI-38 responses remained minimal and relatively unchanged. Overall, these findings indicate that prolonged MMW irradiation preferentially induces apoptosis in lung cancer cells, while exerting limited effects on normal lung fibroblasts. Notably, NCI-H1299 cells (p53-null genotype) demonstrated a more pronounced anti-proliferative and pro-apoptotic response compared to A549 cells, suggesting that genetic background may influence cellular sensitivity to MMW exposure.

2.7. MMW Irradiation Induces Senescence-Associated Growth Arrest in Lung Cancer Cells with Limited Effects in Normal Lung Fibroblasts

The most pronounced anti-proliferative effect in lung cancer cells was observed by using the PH antenna, 90–96 GHz frequency without attenuation (4.8 mW) following 60 minutes of MMW irradiation. To assess the long-term biological consequences of MMW irradiation, we combined a reseeding-based long-term survival assay with measurements of senescence-associated β-

 doi:10.20944/preprints202603.1938.v1

galactosidase (SA-β-gal) activity. This combined approach enables discrimination between cells that remain proliferative and cells that survive but enter senescence-associated growth arrest. While cell counting quantifies the total number of surviving cells after reseeding, it does not distinguish between proliferating cells and viable but non-dividing senescent cells. In contrast, SA-β-gal activity reflects the accumulation of senescence-associated features in metabolically active cells. Integration of both assays, therefore, allows estimation of the fraction of cells that retain true functional viability, defined here as survival with preserved proliferative capacity. The results are depicted in the following figure (Figure 6).

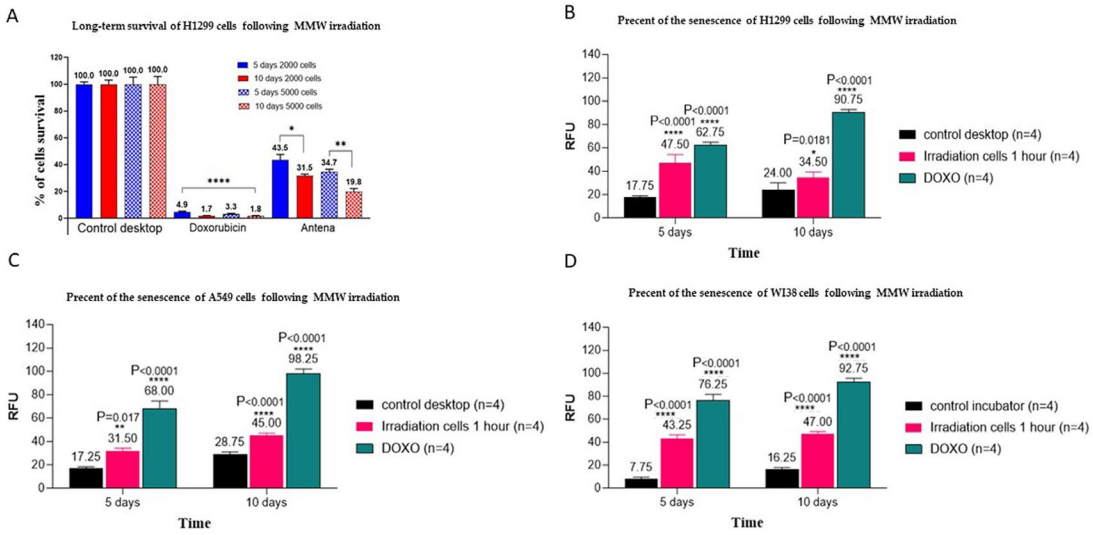

Figure 6. Effects of MMW irradiation on long-term survival and senescence-associated β-galactosidase activity in lung cell lines. **(A)** Long-term survival of NCL-H1299 cells following MMW irradiation. NCL-H1299 cells (250,000 cells per condition) were irradiated and subsequently reseeded at densities of 2,000 or 5,000 cells per well in 24-well plates. The number of surviving cells was counted after 5 and 10 days and expressed as a percentage relative to non-irradiated control cells (100%). Doxorubicin was used as a positive control. Senescence-associated β-galactosidase (SA-β-gal) activity in NCL-H1299 (**B**), A549 lung cancer cells (**C**), and WI-38 normal lung fibroblast cells (**D**), measured after 5 and 10 days following irradiation, respectively. SA-β-gal activity was quantified fluorometrically and was expressed as relative fluorescence units (RFU). WI-38 normal lung fibroblast cells- non-irradiated cells served as negative controls, and doxorubicin (DOXO) was used as a positive control for senescence induction. Data are presented as mean ± SD (n = 4). Significance is indicated as: $p < 0.05$ (*), $p < 0.01$ (**), and $p < 0.001$ (***).

As shown in Figure 6A, MMW irradiation to NCL-H1299 lung cancer cells resulted in a marked reduction in long-term survival following reseeding. Five days after irradiation, approximately 40–45% of cells survived relative to non-irradiated controls. This fraction declined further to ~20–32% by day 10, depending on seeding density. As expected, doxorubicin treatment led to near-complete loss of surviving cells at both time points, consistent with extensive cytotoxicity. In parallel, SA-β-gal activity was significantly elevated in irradiated NCL-H1299 cells (Figure 6B). On day 5 (post-irradiation), SA-β-gal activity increased approximately 2–3-fold relative to controls, indicating induction of a senescence-associated phenotype within the surviving population. Although SA-β-gal activity remained elevated on day 10, it was substantially lower than that induced by doxorubicin. This suggested the partial, rather than uniform, senescence induction.

Importantly, the senescent cells remain viable and metabolically active. Hence, they were included in survival counts despite lacking proliferative capacity. Based on the magnitude of SA-β-gal induction, we conservatively estimate that approximately 30–40% of the surviving NCL-H1299 cells had entered senescence-associated growth arrest by day 5. When this fraction is excluded, the proportion of cells retaining proliferative capacity is reduced from an apparent survival of ~45% to

 doi:10.20944/preprints202603.1938.v1

an estimated functional viability of ~25–30% at this time point. By day 10, overall survival was further reduced (Figure 6A), while SA-β-gal activity remained elevated (Figure 6B), indicating persistence of senescence-associated growth arrest among the remaining cells. At this later time point, we estimated that ~ 40–50% of surviving cells exhibit senescence-associated features, yielding an estimated functional viability of only ~10–15% of the original population.

Consistent with this interpretation, MMW irradiation induced similar increases in SA-β-gal activity in A549 lung cancer cells (Figure 6C), indicating that senescence-associated growth arrest contributes broadly to reduced long-term proliferative capacity in lung cancer cell lines. These findings complement our apoptosis and survival data, together suggesting that MMW irradiation limits cancer cell expansion through a combined effect of early cell death and delayed senescence-associated growth arrest among surviving cells.

In contrast, WI-38 normal lung fibroblasts exhibited a more moderate increase in SA-β-gal activity following irradiation (Figure 6D). Importantly, WI-38 cells are a finite, non-immortalized cell line that is intrinsically prone to replicative and culture-associated senescence, particularly after repeated passaging [16–18]. The modest elevation in SA-β-gal activity observed in WI-38 cells is, therefore, consistent with a mild stress- or passage-associated response rather than extensive cytotoxicity or irreversible growth arrest. This interpretation is further supported by the absence of pronounced cell loss in long-term survival assays and by the substantially weaker SA-β-gal induction compared with doxorubicin.

Together, these results demonstrate that MMW irradiation primarily restricts long-term expansion of lung cancer cells through a combination of cell death and senescence-associated growth arrest, while exerting only modest, non-cytotoxic stress effects in normal lung fibroblasts. Integration of survival and senescence assays reveal that the fraction of cells retaining true proliferative potential after irradiation is substantially lower than suggested by cell counts alone.

3. Discussion

3.1. Defining Non-Thermal MMW Irradiation in a 3D Tumor Model

Previous work from our group demonstrated that MMW irradiation (75-110 GHz) at relatively low PD (~0.2 mW/cm²) induces selective anti-cancer effects in 2D human lung cancer cells and budding yeast, with cancer cells showing markedly higher sensitivity than their normal counterparts [9,12]. Recent studies revealed that high-frequency MMW of electromagnetic radiation (51.8 GHz to 73 GHz) had an overall inhibitory effect on bacterial growth [19]. Moreover, the previous studies demonstrated that the effects of 95 and 105 GHz correspond to the resonant frequencies of H_2O molecules, suggesting that these effects are mediated by water [20]. In further advancement of our previous report, in the present study, we developed a physiologically relevant 3D tumor-like spheroid model to define biologically meaningful conditions for MMW irradiation. Unlike conventional 2D systems, this model recapitulates key features of early tumor architecture, such as compact cellular organization, diffusion limitations, and spatial heterogeneity. Computational and geometrical analyses confirmed that spheroids formed with 10–20 μL droplets display predictable dimensions and structural gradients, which allow controlled investigation of depth-dependent electromagnetic effects (Figure 2). A central observation emerging from this system is the inherently non-uniform distribution of MMW energy within the spheroid. Due to exponential attenuation in biological media, energy deposition is highest at the surface and decreases with depth, as demonstrated in Figure 2 and supported by quantitative estimates (see Table 1). Importantly, these gradients persist even under near-field exposure conditions, indicating that depth-dependent energy delivery is an intrinsic property of MMW–tissue interaction rather than an experimental limitation. The irradiation was performed under active cooling (~15 °C; Figure 2) to ensure non-thermal conditions and ensure negligible bulk temperature increase. Under these conditions, most of the incident energy is absorbed within the superficial layers (≤0.5 mm), supporting the conclusion that

 doi:10.20944/preprints202603.1938.v1

the observed biological responses arise primarily from direct electromagnetic interactions rather than thermal effects.

3.2. Integration of Physical Parameters with Biological Outcomes

Cell density emerged as a critical modulator of MMW sensitivity in 3D tumor-like spheroid model (Figure 3). Lower-density cultures (5×10^3 cells/10 μL) consistently exhibited the strongest reductions in both acute viability and long-term clonogenic survival, particularly under prolonged exposure (see Figure 3). This sharp sensitivity likely reflects reduced shielding effects and increased per-cell energy absorption in sparsely populated droplets. In contrast, intermediate cell densities (1×10^4 cells/10 μL) showed partial resistance to short-term exposure, suggesting that collective cellular organization and local microenvironmental buffering can transiently mitigate MMW-induced stress (see Figure 3). These findings suggested that the cell density must be considered a defining experimental and biological variable when evaluating MMW effects in 3D systems. Importantly, these results indicate that in real 3D tumors, irradiation conditions need to be tailored to tumor size, cellular density, and structural heterogeneity to achieve optimal therapeutic efficacy.

Comparative analysis of antenna systems further revealed that power density (PD) and frequency bandwidth—rather than exposure duration alone—are the primary determinants of treatment efficacy (Figure 4). Both WG and PH antennas produced measurable anti-proliferative effects. WG produces strong cytotoxicity at low PD due to its concentrated field, whereas PH—designed to irradiate a larger area and more cells—requires modulation of attenuation to achieve similar biological effects. The most pronounced and sustained responses were observed with the PH antenna coupled to a frequency multiplier, which delivered a substantially higher localized PD (~4.9 mW/cm²) within a narrower frequency window (90–96 GHz) in 3D spheroid models (5,000–250,000 cells). This contrasts with our previously published WG-based irradiation of yeast cells, which operated across a broader frequency range (75–110 GHz) at lower PD (~0.2 mW/cm²) and lower cell density (5,000 cells) [13]. Together, these findings indicate that antenna geometry and sufficient electromagnetic field strength are essential for achieving consistent and reproducible biological outcomes, even when exposure duration is held constant.

Importantly, MMW irradiation demonstrated cancer-selective activity across lung cell types with distinct genetic and phenotypic backgrounds (Figure 5). Highly proliferative, p53-deficient NCL-H1299 cells were the most sensitive, followed by p53-wild-type A549 cells, whereas normal WI-38 lung fibroblasts exhibited substantially higher survival and minimal apoptosis. This selectivity was preserved across exposure durations and antenna configurations and was further supported by apoptosis assays, which showed preferential induction of programmed cell death in cancer cells—particularly under higher PD conditions (Table 3). These results underscore a p53-linked mechanistic divergence in stress response pathways and highlight the potential of MMW irradiation as a selective, nonionizing therapeutic modality for targeting malignant cells while sparing normal tissue.

3.3. Short- and Long-Term Cellular Responses

Beyond acute cytotoxicity, MMW irradiation induced significant long-term effects on cellular proliferation. Integration of reseeding assays with SA β-galactosidase measurements revealed that a large fraction of surviving cells had lost proliferative capacity (Figure 6). Thus, functional viability was markedly lower than indicated by short-term assays alone. This dual response—apoptosis in highly affected cells and senescence in surviving populations—suggests that MMW irradiation disrupts tumor growth through complementary mechanisms. Normal fibroblasts exhibited only modest increases in senescence markers, consistent with a reversible stress response rather than irreversible damage. Importantly, NCI-H1299 cells exhibited significantly greater sensitivity compared to A549 cells, with higher levels of both apoptosis and long-term proliferative arrest. In contrast, A549 cells retained partial proliferative capacity, suggesting a more adaptive or resistant phenotype. This divergence highlights the influence of genetic background, particularly p53 status, on cellular response to MMW exposure.

 doi:10.20944/preprints202603.1938.v1

Our findings are consistent with previous reports demonstrating differential sensitivity between lung cancer cell lines with distinct genetic backgrounds. Notably, human lung cancer NCI-H1299 (p53-null) cells have been shown to exhibit enhanced susceptibility to DNA damage–inducing agents compared to A549 (p53 wild-type) cells. A study published in the International Journal of Molecular Sciences (2018) and others demonstrated that H1299 cells display hypersensitivity to 8-chloro-adenosine due to accumulation of DNA double-strand breaks, impaired DNA repair capacity, and defects in the p53–p21 signaling pathway. In contrast, A549 cells retain more effective DNA damage response mechanisms, allowing improved repair and survival [21,22]. These mechanistic insights are in strong agreement with our observations. In the present study, NCI-H1299 cells exhibited significantly higher levels of apoptosis and long-term growth arrest following MMW irradiation compared to A549 cells. This suggests that MMW-induced stress may similarly engage DNA damage–related pathways, to which p53-deficient cells are more vulnerable due to compromised repair capacity.

The agreement between these findings and our results suggests that MMW-induced stress may converge on DNA damage–related pathways, to which p53-deficient cells are particularly vulnerable. Thus, the enhanced sensitivity of H1299 cells likely reflects underlying DNA damage-related deficiencies, supporting the central role of genetic background in determining response to MMW exposure. From a translational perspective, these results support MMW irradiation as a modality capable of inducing both acute tumor cell death and sustained growth inhibition. The observed genotype-dependent responses further emphasize the need for personalized optimization of irradiation parameters, in line with precision oncology approaches.

3.4. Mechanistic Model: From Surface Energy Deposition to Intracellular Damage

To integrate these findings, we propose a depth- and receptor-mediated mechanistic model (Figure 7).

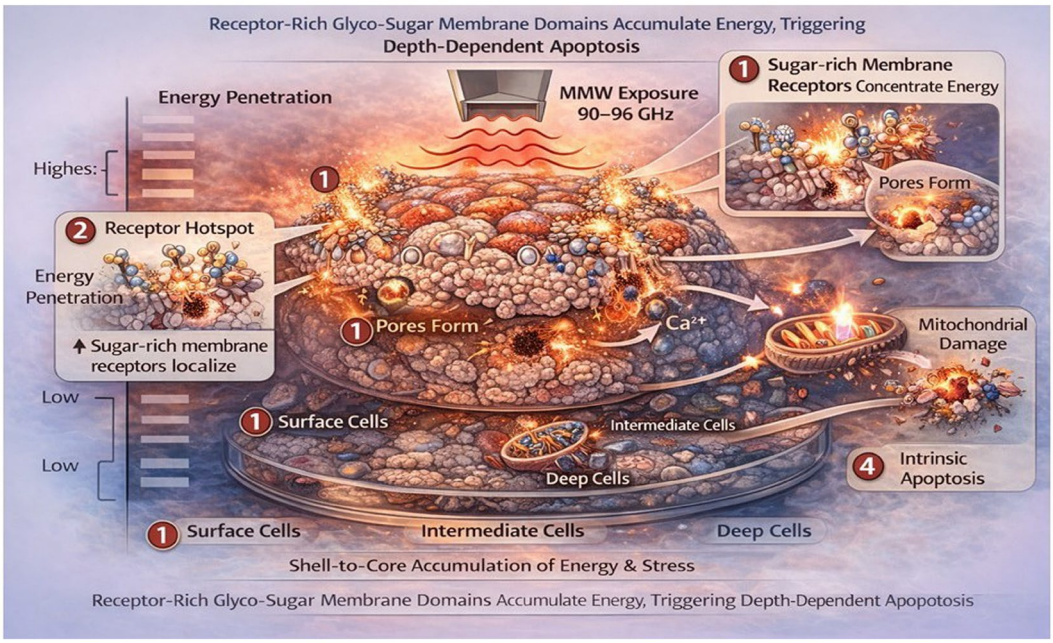

Figure 7. Mechanistic model of MMW irradiation in a 3D tumor-like spheroid emphasizing receptor-mediated energy accumulation. The above figure (Figure 8) represents a 3D tumor spheroid under MMW exposure. MMW energy penetrates the spheroid and preferentially interacts with sugar-rich membrane receptors (yellow), leading to localized energy accumulation. This accumulation may cause nano-scale membrane disruptions ("holes," red), enhancing calcium influx and triggering intracellular stress responses. Superficial cells experience the highest energy deposition, resulting in Reactive Oxygen Species (ROS) generation, mitochondrial stress, and

 doi:10.20944/preprints202603.1938.v1

DNA damage (light blue nuclei and mitochondria). The energy gradient diminishes with depth, producing progressive, layer-dependent apoptosis. Color-coded arrows indicate energy penetration, receptor-mediated hotspot formation, and downstream signaling. Normal fibroblasts (green) are less affected due to intact membrane integrity and more robust antioxidant defenses.

MMW energy forms a gradient within the spheroid, with the highest absorption on the surface. At the cellular level, energy preferentially interacts with glycosylated membrane domains, potentially creating localized electromagnetic "hotspots." These regions may undergo transient nano-scale perturbations, increasing membrane permeability and enabling calcium influx [23–25]. This initiates intracellular stress cascades, including ROS generation, mitochondrial dysfunction, and DNA damage [26–29]. Cancer cells, characterized by elevated basal ROS, altered membrane composition, and impaired stress responses, are more susceptible to cumulative damage. In particular, p53-deficient cells lack efficient checkpoint control, enhancing sensitivity to sustained electromagnetic stress [15,30]. The depth-dependent attenuation of energy explains the spatial progression of damage, with apoptosis initiating in superficial layers and extending inward during prolonged exposure. This cumulative, non-thermal stress model aligns with previous reports demonstrating time-dependent biological effects of MMW irradiation without measurable heating [13,31].

Collectively, these findings proposed that the non-ionizing, non-thermal MMW irradiation can selectively suppress lung cancer cell growth in 3D tumor-like models through spatially resolved electromagnetic interactions, without inducing comparable damage in normal lung cells. The convergence of density-dependent sensitivity, antenna-specific energy delivery, genotype-dependent susceptibility, and long-term senescence induction supports the potential of MMW irradiation as a precise, non-invasive anti-cancer strategy. Importantly, these results also provide a rational framework for optimizing irradiation parameters in future translational studies, emphasizing that biological outcome is determined not by exposure to time alone, but by the integrated physical and cellular context.

4. Materials and Methods

4.1. Cell Culture

Human lung cancer cell lines NCI-H1299 and A549, along with non-cancerous human lung fibroblasts WI-38 (ATCC CCL-75™), were obtained from the American Type Culture Collection (ATCC, Israel). NCI-H1299 is an aggressive lung carcinoma cell line lacking functional TP53, while A549 is a less aggressive lung adenocarcinoma line expressing wild-type TP53 and harboring KRAS mutations.

Cells were cultured as follows: NCI-H1299: RPMI-1640 medium (Gibco, Thermo Fisher Scientific, Waltham, MA, USA) supplemented with 10% fetal bovine serum (FBS), 2 mM L-glutamine, and 1% penicillin/streptomycin (Sigma-Aldrich, St. Louis, MO, USA). A549: Dulbecco's Modified Eagle's Medium (DMEM; Gibco) with 10% FBS, 2 mM L-glutamine, and 1% penicillin/streptomycin. WI-38: Minimum Essential Medium Alpha Modification (MEM; HyClone, Thermo Scientific) supplemented with 10% FBS. Cells were seeded in 96-well plates at 2×10^4 cells per 100 µL or in 6-well plates at 1×10^6 cells per 2 mL for subsequent assays.

4.2. MMW Irradiation Set-up and 3D Model of Study

The experimental setup was based on a W-band source feeding two types of radiating apparatus: a pyramidal horn (PH) antenna and an open waveguide (WG) probe, as schematically shown in Figure 8, with irradiation conditions summarized in Table 3. A signal generator (Agilent 83632B) producing a tunable RF signal at 10 MHz–20 GHz is followed by an x6 frequency multiplier (Quinstar QMM-940615060), producing a millimeter wave radiation at W-band (75-110 GHz). A variable 0–60 dB attenuator (Quinstar QAD-W00000) was employed to control the MMW radiated power.

 doi:10.20944/preprints202603.1938.v1

The emitted radiation was delivered to the cells via either a WG probe (2.5 × 1.75 mm; aperture 4.37 mm²) or a PH antenna (7 × 4.75 mm; aperture 32.9 mm²). The WG probe provided highly localized irradiation with relatively high-power density across the 75–110 GHz range, whereas the PH antenna enabled irradiation over a substantially larger area but at lower baseline power density.

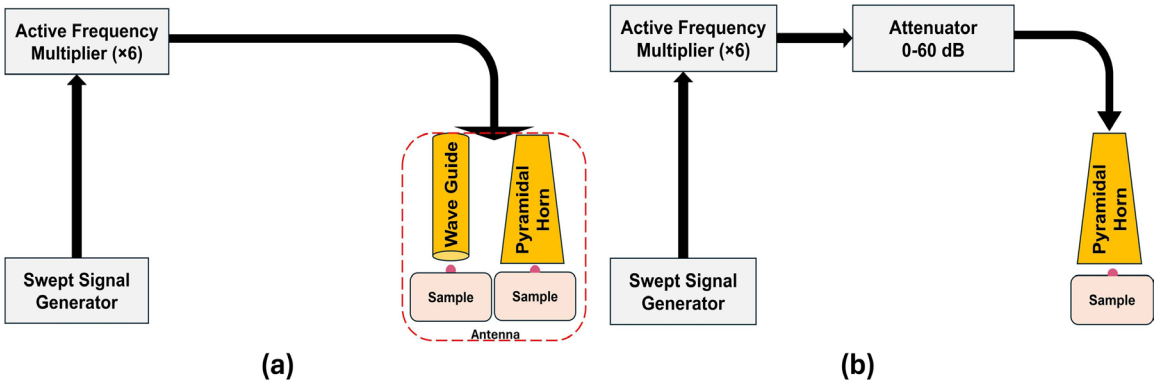

Figure 8. Schematic representation of the millimeter-wave (MMW) irradiation setup. (a) Figure 8. Schematic representation of the millimeter-wave (MMW) irradiation setup. (a) The system comprises a swept signal generator (10 MHz–20 GHz; Agilent 83632B) feeding a solid-state active multiplier (Quinstar QMM-940615060; ×6), connected to one of two antenna types with distinct aperture sizes: a waveguide probe (2.5 × 1.75 mm; aperture 4.37 mm²) or a pyramidal horn (7 × 4.75 mm; aperture 32.9 mm²). This configuration generates an output frequency range of 75–110 GHz, corresponding to wavelengths (λ) of 4.0–2.725 mm. **(b)** The system includes a swept signal generator connected to the same solid-state active multiplier (×6) and coupled via an attenuator to a pyramidal horn (PH), enabling precise regulation of MMW power. This configuration operates within a narrower frequency range of 90–96 GHz, with and without attenuation.

To enhance the power output of the PH configuration, the system was optimized by operating within a narrower frequency range (90–96 GHz) and by incorporating an attenuator Figure 8b. Under these conditions, and without attenuation, the power density increased from 0.076 mW/cm² to 4.9 mW/cm². Due to the pyramidal geometry, the PH antenna produced a non-uniform spatial power distribution, with maximal intensity at the center and gradual attenuation toward the periphery.

Cell irradiation setup and protocol are presented in Figures 9 and 10. Cells were detached and resuspended as small-volume droplets (10–20 µL; 5 × 10^3–2.5 × 10^5 cells) placed at the center of sterile 35 mm Petri dishes to form three-dimensional (3D) cell clusters mimicking tumor architecture Figure 9c. Low- and high-power, frequency-scanning MMW radiations were applied using either the PH or WG antenna (Figures 8–10; summarized in Table 3) across the W-band (75–110 GHz) with exposure durations of 15, 30, and 60 min. In the optimized PH configuration, the frequency range was restricted to 90–96 GHz, resulting in an approximately tenfold increase in power density compared to baseline conditions. The PH antenna produced a Gaussian-like spatial distribution, with maximal intensity at the center and decreasing toward the edges, whereas the WG probe generated a confined, high-intensity focal region.PH or WG antenna (Figure 8, 9a and b, and summarized Table 3). To minimize thermal effects, samples were maintained on a cooled surface (~4–6 °C) during irradiation.

 doi:10.20944/preprints202603.1938.v1

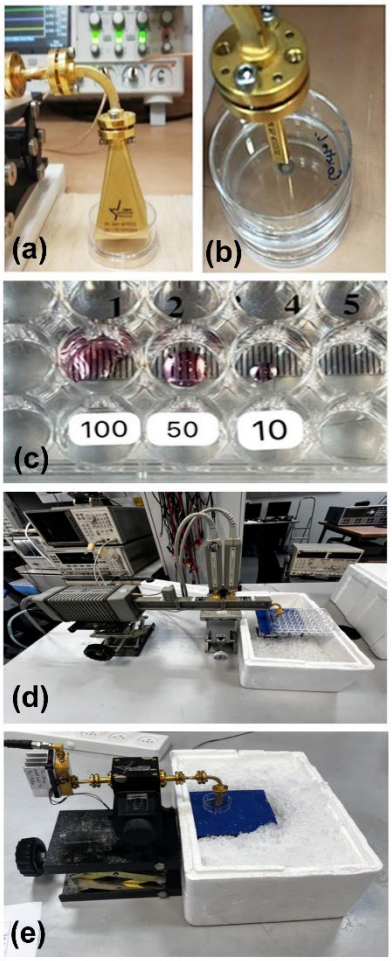

Figure 9. Representative experimental exposure setup images: **(a)** PH antenna; **(b)** WG antenna; **(c)** Cancer cell droplets (5×10^3 cells/10 mL-2.5×10^4 cells/20 mL); **(d–e)** Irradiation layout showing plates on ice (4–6 °C).

Acute effects on cell viability were assessed using the Enhanced Cell Counting Kit-8 (E-CK-A362-500, Elabscience). Apoptotic cell fractions were quantified using the MEBCYTO Annexin V–FITC Apoptosis Detection Kit (cat# 4700, ENCO) by flow cytometry (FACS).

Chronic effects of MMW irradiation on cell survival and proliferative capacity were evaluated using a clonogenic (colony formation) assay, together with assessment of senescence-associated β-galactosidase (SA-β-gal) activity. This combined approach enables discrimination between proliferating cells and those that remain viable but undergo senescence-associated growth arrest.

An overview of the experiment schedule is depicted in Figure 10.

 doi:10.20944/preprints202603.1938.v1

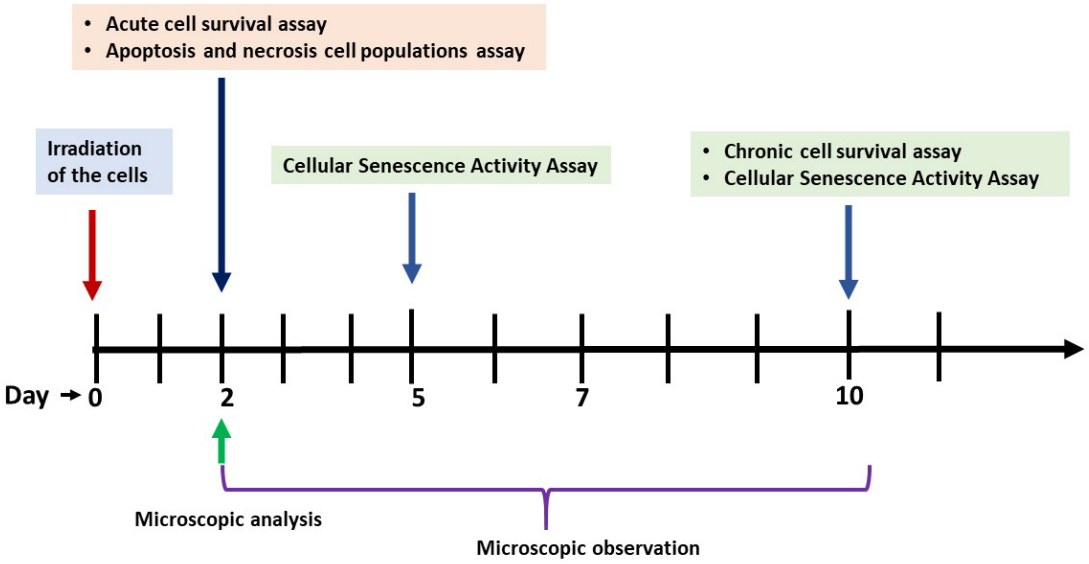

Figure 10. Experimental design overview. Acute effects (Day 2) were assessed using XTT and FACS apoptosis assays; chronic effects (Days 10–12) were evaluated by colony formation assays (CFA), measurement of senescence-associated β-galactosidase (SA-β-gal) activity, and microscopy.

Key specifications of both antennas, including aperture area, power level, and power density (PD) per unit area, are summarized in Table 3.

Table 3. Irradiation Regimes and antenna characteristics.: Summary of antenna type, aperture size and area, frequency range, power level (dBm and W), power density (mW/cm²), and exposure duration.

Radiation source	Antenna type	Antenna size (mm)	Aperture area (mm2)	Irradiation type	Irradiation range (GHz)	Range power level	Average power density (mW/cm²)	Exposure time (min)
Swept Signal Generator + Frequency multiplier	Wage guide probe	2.5 × 1.75	4.37	Sweeping regime	75-110	-2 dBm 0.63 mW	0.576	15, 30, 60
Swept Signal Generator +Frequency multiplier	Pyramidal	7.0 × 4.7	32.9				0.076	
Swept Signal Generator + Generator +Frequency multiplier + Attenuator								
Swept Signal Generator + Frequency multiplier r + witAttenuator without attenuation					90-96	16 dBm, 40 mW	4.86	

Low-power irradiation: W-band (75–110 GHz), tunable output up to 10 mW, exposure durations 10, 30, and 60 min. PH antenna with frequency multiplier: Narrowed the range to 90–96 GHz and increased PD tenfold compared to WG. The PH antenna produces a Gaussian energy distribution, with the highest PD at the center and a gradual decrease toward the periphery. In contrast, WG produces a focused beam restricted to a small area. To minimize nonspecific thermal effects, plates

 doi:10.20944/preprints202603.1938.v1

were placed on a cold table (≈15 ℃) during irradiation. Irradiation effects were evaluated at two time points: acute (2 days) and chronic (10 days)

4.3. Cell Viability Assay

Cell viability 48 h after MMW irradiation was assessed using the Enhanced Cell Counting Kit-8 (E-CK-A362-500, Elabscience). Post-irradiation, 5,000 cells were seeded in 96-well plates with 4–6 replicates per condition. Assays were performed following the manufacturer's instructions. Positive control: Doxorubicin (100 nM). Negative controls: (1) untreated cells (non-irradiated/sham), (2) cells handled identically but not irradiated ("handling control"). The assay measured the acute impact of MMW treatment on lung cancer cell viability.

4.4. Clonogenic Assay

Long-term effects of MMW irradiation on cell survival, proliferation, and colony-forming ability were assessed using a clonogenic assay. Post-irradiated cells (500–1,000, depending on cell line) were seeded in 35 mm Petri dishes. After ~10 days, when colonies were optimally grown, cells were fixed with 100% ethanol (10 min) and stained with 0.05% crystal violet. Colonies were washed with distilled water and counted to evaluate the chronic effects of MMW exposure. All experiments were performed at least four times per cell line to ensure reproducibility.

4.5. Microscopy And Image Processing

The effects of MMW exposure on lung cancer cell morphology were analyzed using a Nikon fluorescent microscope (Nikon Instruments Inc., Melville, NY) at 200× magnification. Images were captured with a Hamamatsu digital color-cooled camera (Bridgewater, NJ) and viewed using NIS Elements software (Nikon Instruments Inc.). For image analysis and processing, ImageJ (NIH, Bethesda, MD) was used to quantify morphological changes, including cell size, shape, and cluster formation.

4.6. Flow Cytometry

Apoptosis was evaluated immediately after MMW irradiation using the MEBCYTO Annexin V–FITC Apoptosis Detection Kit (cat# 4700, ENCO). Cells were stained with Annexin V-FITC and propidium iodide (PI) following the manufacturer's instructions. Data acquisition was performed using a CytoFlex S flow cytometer (Beckman Coulter, Brea, CA, USA), analyzing 1,000,000 cells per sample. All experiments were conducted in triplicate. FITC fluorescence was excited at 488 nm and collected at 525/40 nm, while LIVE/DEAD IR was excited at 638 nm and collected at 780/60 nm. Data was processed using FlowJo 10.0.7 software (Treestar Inc., Ashland, OR, USA) to determine the proportion of apoptotic, necrotic, and viable cells. This assay quantified acute apoptotic responses in cells following MMW irradiation.

4.7. Cellular Senescence Activity Assay

The cells were seeded in 24-well plates at a density of 2,000 cells/well, with media changes performed every other day. On days 5 and 10, cells were harvested, and protein content (for sample normalization) was analyzed using the Pierce BCA Protein Assay Kit (23227, Thermo Fisher Scientific, USA). SA-β-galactosidase activity was then assessed using the Cellular Senescence Assay Kit t (# ENZ-KIT12923227, Enzo Life Sciences, USA). It used the β-gal Substrate 4-Methylumbelliferyl β-D-galactopyranoside (4-MUG) to detect Senescence-Associated beta-galactosidase (SA-β-gal) activity. Upon binding to β-gal, 4-MUG is hydrolyzed to the fluorescent product 4-MU that can be measured at an excitation wavelength of 360 nm and an emission wavelength of 465 nm. Fluorescent intensity correlates with sample β-gal levels. This quantitative assay uses cellular lysates for the determination of SA-β-gal activity.

 doi:10.20944/preprints202603.1938.v1

4.8. Statistical Analysis

All experiments were performed in at least three independent replicates (n ≥ 3-6). Data are presented as mean ± standard deviation (SD). Statistical comparisons between groups were performed using Student's t-test or one-way ANOVA where appropriate. A p-value < 0.05 was considered statistically significant.

5. Conclusions

This study demonstrates that non-ionizing, non-thermal MMW irradiation can selectively suppress lung cancer cell growth within a 3D tumor-like environment under well-controlled physical conditions. The results indicate that MMW exposure generates a predictable, depth-dependent energy gradient that drives spatially distinct cellular responses. These biological outcomes are governed by integrated parameters, including power density, exposure duration, antenna configuration, and cell density. MMW treatment induces both apoptosis and senescence, leading to a substantial reduction in long-term tumor viability, with p53-deficient cells exhibiting the highest sensitivity. Mechanistically, the findings support a model involving membrane-associated energy accumulation followed by calcium influx, ROS generation, mitochondrial dysfunction, and DNA damage. Overall, this study establishes a mechanistic and experimental foundation for advancing MMW irradiation as a precise, non-invasive anti-cancer modality. Future work should focus on direct molecular validation of calcium-, ROS-, and mitochondria-dependent pathways, as well as the optimization of irradiation parameters for translational and clinical applications

Author Contributions: Conceptualization, S.L-A. and A.Y.; methodology, S. L-A., H.T., A.Y., Y.P., B.L., V.F.; validation and statical analysis, H.T. and S.L-A., investigation resources, , S. L-A, A.Y. and Y.P.; data curation, S. L-A., writing—original draft preparation, S.L-A. and D. P.; writing—review and editing, S. L-A., A.Y., Y.P., D.P., supervision, S. L-A., A.Y., Y.P.; project administration . S. L-A and A. Y., funding acquisition, S. L-A., A.Y. All authors have read and agreed to the published version of the manuscript.

Funding: This research was partially funded by the Israeli Ministry of Health grant # 20230409 "Cancer treatment using millimeter waves".

Institutional Review Board Statement: Not applicable.

Consent Statement: Not applicable.

Data Availability Statement: The original contributions presented in this study are included in the article. Further inquiries can be directed to the corresponding author.

Conflicts of Interest: The authors declare no conflicts of interest.

Abbreviations

The following abbreviations are used in this manuscript:

MEM: Minimum essential medium, µL: Microliter, mL: Milliliter, mm: Millimeter, PH: Pyramidal horn, WG: Waveguide, mW: Milliwatt, ℃: Degree centigrade Celsius, h: Hours, nM: Nanomolar, XTT: 2,3-bis(2-methoxy-4-nitro-5-sulfophenyl)-5-carboxanilide-2H-tetrazolium, nm: Nanometer, ANOVA: Analysis of variance, SD: Standard deviation, cm: Centimeter, µm: Micrometer, PD: Power density, mJ: Millijoule, CFA: Colony formation assay, ROS: Reactive oxygen species.

References

1. Siegel, R.L.; Miller, K.D.; Jemal, A. Cancer Statistics, 2020. *CA A Cancer J Clinicians* **2020**, *70*, 7–30. https://doi.org/10.3322/caac.21590.

 doi:10.20944/preprints202603.1938.v1

2. Sung, H.; Ferlay, J.; Siegel, R.L.; Laversanne, M.; Soerjomataram, I.; Jemal, A.; Bray, F. Global Cancer Statistics 2020: GLOBOCAN Estimates of Incidence and Mortality Worldwide for 36 Cancers in 185 Countries. *CA A Cancer J Clinicians* **2021**, *71*, 209–249. https://doi.org/10.3322/caac.21660.
3. Bray, F.; Ferlay, J.; Soerjomataram, I.; Siegel, R.L.; Torre, L.A.; Jemal, A. Global Cancer Statistics 2018: GLOBOCAN Estimates of Incidence and Mortality Worldwide for 36 Cancers in 185 Countries. *CA A Cancer J Clinicians* **2018**, *68*, 394–424. https://doi.org/10.3322/caac.21492.
4. Herbst, R.S.; Morgensztern, D.; Boshoff, C. The Biology and Management of Non-Small Cell Lung Cancer. *Nature* **2018**, *553*, 446–454. https://doi.org/10.1038/nature25183.
5. Jang, J.Y.; Kim, D.; Im, E.; Kim, N.D. Etoposide as a Key Therapeutic Agent in Lung Cancer: Mechanisms, Efficacy, and Emerging Strategies. *IJMS* **2025**, *26*, 796. https://doi.org/10.3390/ijms26020796.
6. Edmondson, R.; Broglie, J.J.; Adcock, A.F.; Yang, L. Three-Dimensional Cell Culture Systems and Their Applications in Drug Discovery and Cell-Based Biosensors. *ASSAY and Drug Development Technologies* **2014**, *12*, 207–218. https://doi.org/10.1089/adt.2014.573.
7. Zanoni, M.; Piccinini, F.; Arienti, C.; Zamagni, A.; Santi, S.; Polico, R.; Bevilacqua, A.; Tesei, A. 3D Tumor Spheroid Models for in Vitro Therapeutic Screening: A Systematic Approach to Enhance the Biological Relevance of Data Obtained. *Sci Rep* **2016**, *6*, 19103. https://doi.org/10.1038/srep19103.
8. Jing, R.; Jiang, Z.; Tang, X. Advances in Millimeter-Wave Treatment and Its Biological Effects Development. *IJMS* **2024**, *25*, 8638. https://doi.org/10.3390/ijms25168638.
9. Radzievsky, A.A.; Gordiienko, O.V.; Szabo, I.; Alekseev, S.I.; Ziskin, M.C. Millimeter Wave-induced Suppression of B16 F10 Melanoma Growth in Mice: Involvement of Endogenous Opioids. *Bioelectromagnetics* **2004**, *25*, 466–473. https://doi.org/10.1002/bem.20018.
10. Beneduci, A.; Chidichimo, G.; Rose, R.D.; Filippelli, L.; Straface, S.V.; Venuta, S. Frequency and Irradiation Time-Dependant Antiproliferative Effect of Low-Power Millimeter Waves on RPMI 7932 Human Melanoma Cell Line. *ANTICANCER RESEARCH* **2005**.
11. Beneduci, A. Evaluation of the Potential In Vitro Antiproliferative Effects of Millimeter Waves at Some Therapeutic Frequencies on RPMI 7932 Human Skin Malignant Melanoma Cells. *Cell Biochem Biophys* **2009**, *55*, 25–32. https://doi.org/10.1007/s12013-009-9053-8.
12. Zhao, R.; Liu, Y.; Liu, S.; Luo, T.; Zhong, G.Y.; Liu, A.; Zeng, Q.; Xin, S.X. Apoptosis-Promoting Effects on A375 Human Melanoma Cells Induced by Exposure to 35.2-GHz Millimeter Wave. *Technol Cancer Res Treat* **2020**, *19*, 1533033820934131. https://doi.org/10.1177/1533033820934131.
13. Komoshvili, K.; Israel, K.; Levitan, J.; Yahalom, A.; Barbora, A.; Liberman-Aronov, S. W-Band Millimeter Waves Targeted Mortality of H1299 Human Lung Cancer Cells without Affecting Non-Tumorigenic MCF-10A Human Epithelial Cells In Vitro. *Applied Sciences* **2020**, *10*, 4813. https://doi.org/10.3390/app10144813.
14. Geva, P.; Komoshvili, K.; Liberman-Aronov, S. Two- and Three-Dimensional Tracking of MFA2 mRNA Molecules in Mating Yeast. *Cells* **2020**, *9*, 2151. https://doi.org/10.3390/cells9102151.
15. Barbora, A.; Rajput, S.; Komoshvili, K.; Levitan, J.; Yahalom, A.; Liberman-Aronov, S. Non-Ionizing Millimeter Waves Non-Thermal Radiation of Saccharomyces Cerevisiae—Insights and Interactions. *Applied Sciences* **2021**, *11*, 6635. https://doi.org/10.3390/app11146635.
16. Hayflick, L.; Moorhead, P.S. The Serial Cultivation of Human Diploid Cell Strains. *Experimental Cell Research* **1961**, *25*, 585–621. https://doi.org/10.1016/0014-4827(61)90192-6.
17. Dimri, G.P.; Lee, X.; Basile, G.; Acosta, M.; Scott, G.; Roskelley, C.; Medrano, E.E.; Linskens, M.; Rubelj, I.; Pereira-Smith, O. A Biomarker That Identifies Senescent Human Cells in Culture and in Aging Skin in Vivo. *Proc. Natl. Acad. Sci. U.S.A.* **1995**, *92*, 9363–9367. https://doi.org/10.1073/pnas.92.20.9363.
18. Campisi, J.; d'Adda Di Fagagna, F. Cellular Senescence: When Bad Things Happen to Good Cells. *Nat Rev Mol Cell Biol* **2007**, *8*, 729–740. https://doi.org/10.1038/nrm2233.
19. Hegazy, E.A.; El-Antrawy, M.A. Impact of High Frequency Electromagnetic Radiation on Bacterial Survival and Antibiotic Activity in Exposed Bacteria. *Sci Rep* **2025**, *15*, 7852. https://doi.org/10.1038/s41598-025-90599-8.
20. Tadevosyan, H.; Kalantaryan, V.; Trchounian, A. Extremely High Frequency Electromagnetic Radiation Enforces Bacterial Effects of Inhibitors and Antibiotics. *Cell Biochem Biophys* **2008**, *51*, 97–103. https://doi.org/10.1007/s12013-008-9020-9.

 doi:10.20944/preprints202603.1938.v1

21. Yang, S.-Y.; Li, Y.; An, G.-S.; Ni, J.-H.; Jia, H.-T.; Li, S.-Y. DNA Damage-Response Pathway Heterogeneity of Human Lung Cancer A549 and H1299 Cells Determines Sensitivity to 8-Chloro-Adenosine. *IJMS* **2018**, *19*, 1587. https://doi.org/10.3390/ijms19061587.
22. Gong, X.; Zhou, Y.; Deng, Y. Targeting DNA Damage Response-Mediated Resistance in Non-Small Cell Lung Cancer: From Mechanistic Insights to Drug Development. *Current Oncology* **2025**, *32*, 367. https://doi.org/10.3390/curroncol32070367.
23. Pakhomov, A.G.; Akyel, Y.; Pakhomova, O.N.; Stuck, B.E.; Murphy, M.R. Current State and Implications of Research on Biological Effects of Millimeter Waves: A Review of the Literature. *Bioelectromagnetics* **1998**, *19*, 393–413. https://doi.org/10.1002/(SICI)1521-186X(1998)19:7<393::AID-BEM1>3.0.CO;2-X.
24. Zhadobov, M.; Chahat, N.; Sauleau, R.; Le Quement, C.; Le Drean, Y. Millimeter-Wave Interactions with the Human Body: State of Knowledge and Recent Advances. *Int. j. microw. wirel. technol.* **2011**, *3*, 237–247. https://doi.org/10.1017/S1759078711000122.
25. Romanenko, S.; Siegel, P.H.; Wagenaar, D.A.; Pikov, V. Effects of Millimeter Wave Irradiation and Equivalent Thermal Heating on the Activity of Individual Neurons in the Leech Ganglion. *Journal of Neurophysiology* **2014**, *112*, 2423–2431. https://doi.org/10.1152/jn.00357.2014.
26. Yakymenko, I.; Sidorik, E. RISKS OF CARCINOGENESIS FROM ELECTROMAGNETIC RADIATION OF MOBILE TELEPHONY DEVICES.
27. Burlaka, A.P.; Druzhyna, M.O.; Vovk, A.V.; Lukin, S.M. Disordered Redox Metabolism Of Brain Cells In Rats Exposed To Low Doses Of Ionizing Radiation Or Uhf Electromagnetic Radiation. *Exp. Onc.* **2016**, *38*, 238–241. https://doi.org/10.31768/2312-8852.2016.38(4):238-241.
28. Luukkonen, J.; Liimatainen, A.; Juutilainen, J.; Naarala, J. Induction of Genomic Instability, Oxidative Processes, and Mitochondrial Activity by 50 Hz Magnetic Fields in Human SH-SY5Y Neuroblastoma Cells. *Mutation Research - Fundamental and Molecular Mechanisms of Mutagenesis* **2014**, *760*, 33–41. https://doi.org/10.1016/j.mrfmmm.2013.12.002.
29. Sannino, A.; Allocca, M.; Scarfì, M.R.; Romeo, S.; Zeni, O. Protective Effect of Radiofrequency Exposure against Menadione-induced Oxidative DNA Damage in Human Neuroblastoma Cells: The Role of Exposure Duration and Investigation on Key Molecular Targets. *Bioelectromagnetics* **2024**, *45*, 365–374. https://doi.org/10.1002/bem.22524.
30. Vousden, K.H.; Lane, D.P. P53 in Health and Disease. *Nat Rev Mol Cell Biol* **2007**, *8*, 275–283. https://doi.org/10.1038/nrm2147.
31. Habauzit, D.; Le Quément, C.; Zhadobov, M.; Martin, C.; Aubry, M.; Sauleau, R.; Le Dréan, Y. Transcriptome Analysis Reveals the Contribution of Thermal and the Specific Effects in Cellular Response to Millimeter Wave Exposure. *PLoS ONE* **2014**, *9*, e109435. https://doi.org/10.1371/journal.pone.0109435.